Hydrodynamics of gas-liquid Taylor flow in rectangular microchannels

Thomas Abadie, Joelle Aubin, Dominique Legendre, Catherine Xuereb

Hydrodynamics of gas–liquid Taylor flow in rectangular microchannels

Thomas Abadie · Joëlle Aubin · Dominique Legendre · Catherine Xuereb

Abstract The effect of fluid properties and operating conditions on the generation of gas–liquid Taylor flow in microchannels has been investigated experimentally and numerically. Visualisation experiments and 2D numerical simulations have been performed to study bubble and slug lengths, liquid film hold-up and bubble velocities. The results show that the bubble and slug lengths increase as a function of the gas and liquid flow rate ratios. The bubble and slug lengths follow the model developed by Garstecki et al. (Lab chip 6:437–446, 2006) and van Steijn et al. (Chem Eng Sci 62:7505–7514, 2007), however, the model coefficients appear to be dependent on the liquid properties and flow conditions in some cases. The ratio of the bubble velocity to superficial two-phase velocity is close to unity, which confirms a thin liquid film under the assumption of a stagnant liquid film. Numerical simulations confirm the hypothesis of a stagnant liquid film and provide information on the thickness of the liquid film.

Keywords Microchannel · Gas–liquid Taylor flow · Microreactor · Visualisation experiments · Numerical simulation

T. Abadie · D. Legendre
Institut de Mécanique des Fluides CNRS/INPT/UPS, University of Toulouse, Allée du Prof. Camille Soula, 31400 Toulouse, France

T. Abadie · J. Aubin (✉) · C. Xuereb
Laboratoire de Génie Chimique CNRS/INPT/UPS, University of Toulouse, 4 Allée Emile Monso, BP 84-234, 31030 Toulouse, France
e-mail: joelle.aubincano@ensiacet.fr

List of symbols

A	Cross-section area (m^2)
C	Color function (VOF) (−)
d	Diameter (m)
f	Break-up frequency (s^{-1})
$\mathbf{F}_\sigma$	Capillary force (Pa/m)
k	Constant (−)
$l_{1,\infty}$	norms in the spurious currents evaluation (m/s)
L	Length (m)
m	Constant (−)
$\mathbf{n}$	Normal to the interface (−)
P	Pressure (Pa)
Q	Flow rate (m^3/s)
r	Radius (m)
U	Velocity (m/s)
W	Dimensionless velocity (−)
w	Width (m)
x, y	Axis in 2D simulations (−)

Greek letters

α	Volume fraction (−)
$\beta_{1,2}$	Constant (−)
δ	Liquid film thickness (m)
δ_I	Dirac distribution (interface) (−)
ε	Fraction of area (−)
$\lambda_{1,2}$	Constant (−)
μ	Dynamic viscosity (Pa . s)
ρ	Density (kg/m^3)
σ	Surface tension (N/m)
$\mathbf{\Sigma}$	Viscous stress tensor (Pa)

Subscripts

B	Bubble
ch	Channel
G	Gas phase (air)

h Hydraulic
in Gas inlet
L Liquid phase
S Slug
SC Spurious currents
TP Two-phase

Dimensionless numbers

Bo_{TP} Bond number $Bo = \frac{(\rho_L - \rho_G) d_h^2 g}{\sigma}$

Ca_{TP} Capillary number $Ca = \frac{\mu_L U_{TP}}{\sigma}$

Re_{TP} Reynolds number $Re = \frac{\rho_L U_{TP} d_h}{\mu_L}$

We_{TP} Weber number $We = \frac{\rho_L U_{TP}^2 d_h}{\sigma}$

1 Introduction

The interest of the process industries in microreaction technology for process intensification has become increasingly important over the recent years. Amongst the different applications, microreactors are particularly interesting for fast highly exothermic and/or mass transfer limited gas–liquid reactions since heat and mass transfer are remarkably intensified. Although miniaturized devices are already implemented in industry, the engineering methodologies for the design and integration of microreactors in existing processes are still not clearly defined. The development of such methodologies requires fundamental understanding of the physical phenomena that control the process operation and the specificities of equipment design.

To date, research on gas–liquid flow in microchannels has mainly been dedicated to the study of flow patterns in a range of microchannel geometries and the development of flow pattern maps based on superficial gas and liquid velocities (e.g. Triplett et al. 1999; Waelchli et al. 2006; Yue et al. 2007, 2008) or superficial Weber numbers (Akbar et al. 2003). Slug or Taylor flow is the flow configuration that occurs for a large range of flow conditions, from low to average superficial gas and liquid velocities. Taylor flow is characterized by regular sized bubbles that are longer than the microchannel width or diameter and separated by slugs of liquid. The bubbles fill almost all the entire cross-section of the channel and are separated from the wall by a thin liquid layer. Taylor flow in microreactors is an interesting flow regime because it intensifies both mass and heat transfer due to the fluid recirculation generated in the liquid slug (Gupta et al. 2010; Leung et al. 2010; Sobieszuk et al. 2008; Yue et al. 2007, 2008). However, controlling the flow regime and the characteristic size of the gas–liquid dispersion remains a difficult task. These characteristics depend not only on the physical properties of the fluids but also on the operating conditions, the microchannel geometry and material of fabrication.

T-junction geometries are relatively popular for the production of bubbles in microchannels (Garstecki et al. 2006; van Steijn et al. 2007; Yue et al. 2008; Yun et al. 2010) and the correlation of bubble sizes as a function of the superficial gas and liquid flow rates generated in these geometries has been the subject of several works (Garstecki et al. 2006; van Steijn et al. 2007; Yue et al. 2008; Yun et al. 2010). Few studies, however, have dealt with the effects of fluid properties, such as viscosity and surface tension, on bubble generation (Garstecki et al. 2006; Qian and Lawal 2006; Pohorecki and Kula 2008). Under the flow conditions in these studies, bubble size has been shown to be slightly dependent or not at all on viscosity and surface tension.

The liquid film hold-up around Taylor bubbles is also of main importance for heat and mass transfer in microchannels. The knowledge of the amount of liquid surrounding bubbles in small tubes has been studied for a long time (Aussillous and Quéré 2000; Bretherton 1961; Giavedoni and Saita 1997; Han and Shikazono 2009a), since the first experiments in 1961 by Taylor in circular capillaries, and more recently in microchannels of different cross sections (Han and Shikazono 2009b; Kreutzer et al. 2005a, b; Wong et al. 1995; Yun et al. 2010) where correlations of liquid film thickness as a function of various dimensionless numbers have been developed. Nevertheless, the exact relationships between the microsystem parameters (e.g. geometry and fluid properties) and the characteristics of the gas–liquid flow (e.g. bubble velocity, bubble and slug lengths, and liquid film thickness) are still not clear.

The present work aims at improving the fundamental understanding of gas–liquid Taylor flow in microchannels, which will contribute to the design and development of microreactors for the chemical process industries. In particular, the objective of this study is to investigate the effects of the physical properties of the fluids and the flow rates on the characteristics of the Taylor dispersion generated in a T-junction microchannel. Visualisation experiments and direct numerical simulations have been performed to obtain information on the bubble generation mechanism, bubble velocity, bubble and slug lengths, as well as the liquid film surrounding the bubble body.

2 Experimental setup

2.1 Microchannel characteristics

Rectangular cross-section microchannels have been etched through a silicon wafer plate using the deep reactive ionic etching (DRIE) technique, sandwiched between glass wafers and bonded using anodic bonding. The gas and liquid are contacted using a side-entering T-junction as shown in Fig. 1 and the main channel has a meandering

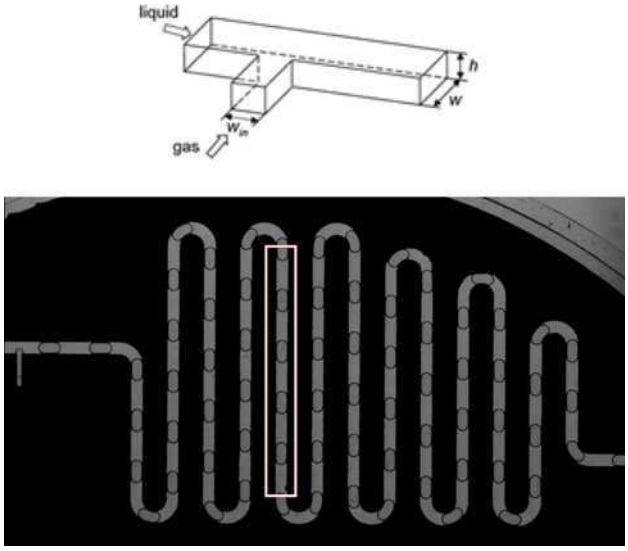

Fig. 1 Side entering T-junction, Meandering microchannel with curved bends, $w_{L,in} = 1$ mm $= w$, $w_{G,in} = 525$ µm, $h = 400$ µm, $d_{h\,=\,571\ \mu m}$, 1–30 cm

topology with curved bends for reasons of compactness. The liquid is flowing in the main channel while the gas is supplied perpendicularly via a narrower channel. The width of the main channel and the gas inlet are $w = 1$ mm and $w_{g,in} = 525$ µm, respectively. The ratio of the widths of the gas and liquid inlets corresponds to the lower limit recommended by Garstecki et al. (2006) for generating Taylor flow via the squeezing mechanism. The depth of the microchannel is fixed by the thickness of the silicon wafer, $h = 400$ µm and the total length is approximately 1–3 cm. These dimensions lead to a hydraulic diameter $d_h = 571$ µm and an aspect ratio $w/h = 2.5$.

2.2 Flow control equipment

Several liquids have been tested to cover a wide range of dimensionless numbers with the feeding equipment available and air has been used as the gas phase for all of the experiments. Air is supplied from a pressurized vessel and controlled by a mass-flow controller (HORIBA SEC 7320), which allows a volumetric flow rate ranging from 0.00 to 1.00 mL/min with a precision of 0.02 mL/min. Liquid flow is controlled using a syringe pump, which allows flow rates in the range of 0.000–1.000 mL/min with a precision of 0.002 mL/min. All experiments were conducted under room temperature and pressure. The temperature of the gas and liquid phases was monitored by thermocouples that are inserted in to the feeding tubes just before the microchannel inlets. The fluid properties are evaluated according to the temperatures measured in each experiment.

2.3 Measurement method

High speed imaging has been used to obtain characteristic information on the gas–liquid Taylor flow. Images have been recorded with a high-speed camera (CCD HCC-1000, VDS Vossmuller GmbH) with frame rates up to 462 fps at full resolution (1024 pix × 1024 pix) and a shutter time short enough to obtain a distinct gas–liquid interface (about 1 ms in our experiments). A backlight was employed to provide enough light throughout the exposure period. A significant number of image sequences were recorded to get a representative sample of bubbles passing through the observation window and to identify unsteady flow situations, which were characterized by irregular bubble lengths.

For the measurement of bubble and slug lengths and bubble velocities, images have been taken in a straight section between two bends and approximately halfway along the length of the channel defined by the rectangular zone shown in Fig. 1. As shown in Fig. 2, the bubble length is evaluated between the extremities of a bubble while the slug length is calculated as the average of the slugs immediately before and after the bubble. From the simulations, the liquid film thickness between the bubble and the walls is characterized by the averaged value along the bulk of the bubble δ, i.e. not including the bubble nose and rear end.

Mean bubble and slug lengths were determined using between 20 and 100 bubbles depending on the flow. Average bubble velocities were evaluated by following the gas–liquid interface at the bubble tip between the entrance and the exit of the observation window, averaging the data of 20–100 bubbles.

2.4 Fluid properties and operating conditions

Reference experiments were carried out using an ethanol-air system, which allows a regular and relatively easy bubble formation in the silicon-glass microchannel (Völkel 2009). The effects of surface tension on bubble generation and hydrodynamics have been studied using water and an ethanol/water solution. Sugarcane syrup solutions (SCS)

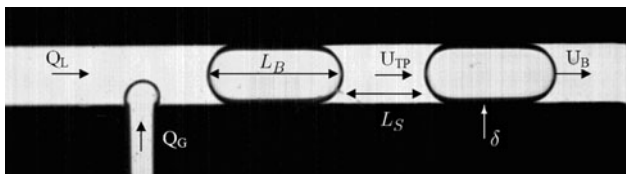

Fig. 2 Contacting section: bubble formation. The notations used are: $Q_{G,L}$ for gas and liquid flow rates, $L_{B,S}$ for bubble and slug lengths, δ the liquid film thickness, U_B the bubble velocity and U_{TP} the superficial two-phase velocity ($U_{TP} = U_L + U_G$)

Table 1 Fluid properties (at room temperature $T = 22$–$23°$ C)

Fluid	ρ_L (kg/m^3)	μ_L(Pa · s)	σ (N/m)
Air	1.204	1.815×10^{-5}	–
Water	998	1.34×10^{-3}	0.068
Ethanol	795	1.15×10^{-3}	0.022
Diluted ethanol (33%)	930	2.4×10^{-3}	0.037
Sugarcane syrup	1,318	1.4×10^{-1}	0.085
Diluted sugarcane syrup (50%)	1,163	4.6×10^{-3}	0.076

have been tested to change the viscosity of the carrier fluid. The properties of the fluids used have been measured and are reported in Table 1. The percentages indicated for ethanol/water and sugarcane syrup/water solutions are volume ratios.

Table 2 summarises the ranges of velocities and dimensionless numbers explored in the experiments. The two-phase dimensionless numbers are based on the physical properties of the liquid and the two-phase velocity, which is the sum of gas and liquid superficial velocities. The superficial velocity is defined as the ratio of the phase flow rate to the channel cross-sectional area, i.e. $U_{L,G} = Q_{L,G}/A_{ch}$.

In terms of dimensionless numbers, the values of the capillary number (ratio of the viscous effects to capillary effects) and the Weber number (ratio of the inertial effects to capillary effects) used in this study indicate that the dominant force in these flows is the capillary force. The Reynolds numbers show that for ethanol, water, ethanol/water and diluted sugarcane syrup, the inertial term dominates the viscous term, howerver this trend is inverted when sugarcane syrup is used. Finally, the Bond number (ratio of the gravitational effects to capillary effects) is less than unity ($Bo_{max} = 0.11$) for all cases and, therefore, the surface tension dominates the gravitational effects. Under these dimensionless flow conditions, and despite the low velocities used, Taylor flow is, therefore, expected since Akbar et al.'s (2003) universal criterion $We_{LS} \leqslant 3$ and $We_{GS} \leqslant 0.11 We_{LS}^{0.315}$ is respected.

3 Numerical simulations

3.1 Governing equations and numerical schemes

The numerical code used for this study is the JADIM code (Dupont and Legendre 2010), which has been developed to simulate dispersed two-phase flows. The interface capturing technique implemented in this code is the volume of fluid method (VOF), which consists of a Eulerian description of each phase on a fixed grid. Under the assumptions that (1) the fluids are Newtonian and incompressible, (2) there is no mass transfer at the interface, (3) the flow is isothermal and (4) the surface tension is constant, the fluid flow can be described by the classical one fluid formulation of the Navier–Stokes equations:

$$\nabla \cdot \mathbf{U} = 0 \tag{1}$$

$$\rho\left(\frac{\partial \mathbf{U}}{\partial t} + (\mathbf{U} \cdot \nabla)\mathbf{U}\right) = -\nabla P + \nabla \cdot \mathbf{\Sigma} + \rho \mathbf{g} + \mathbf{F}_{\sigma,\mathbf{s}} \tag{2}$$

where $\mathbf{\Sigma}$ is the viscous stress tensor ($\mathbf{\Sigma} = \mu(\nabla \mathbf{U} + \nabla \mathbf{U}^T)$), $\mathbf{g}$ is the acceleration due to gravity, $\mathbf{F}_{\sigma,\mathbf{s}} = -\sigma(\nabla \cdot \mathbf{n})\mathbf{n}\delta_I$ is the capillary contribution whose calculation is described below, σ is the surface tension, $\mathbf{n}$ the normal to the interface, δ_I is the Dirac distribution localizing the interface, and ρ and μ are the local density and dynamic viscosity, respectively. The density and viscosity are deduced from the volume fraction of one phase (or colour function) C by a linear interpolation:

$$\rho = C\rho_1 + (1 - C)\rho_2 \tag{3}$$

$$\mu = C\mu_1 + (1 - C)\mu_2 \tag{4}$$

where the volume fraction is $C = 1$ in cells filled with fluid 1, $C = 0$ in cells filled with fluid 2 and $0 < C < 1$ in cells that are cut by the interface. Additionally, the transport equation of the colour function is solved to capture the interface between the phases:

$$\frac{\partial C}{\partial t} + \mathbf{U} \cdot \nabla C = 0 \tag{5}$$

In many VOF methods employed to capture the interface, a reconstruction technique step is used to control the thickness

Table 2 Velocities and dimensionless numbers of the fluids used in the experiments

Fluids	Q_L (mL/min)	Q_G (mL/min)	U_L (10^{-2} m/s)	U_G (10^{-2} m/s)	Re_{TP}	Ca_{TP} 10^{-3}	We_{TP} 10^{-2}	Bo
Air–ethanol	0.2–1	0.04–1	0.83–4.2	0.17–4.2	4–32.9	0.52–4.35	0.21–14	0.115
Air–ethanol (33%)	0.3–1	0.06–1	0.83–4.2	0.17–4.2	3.3–18.5	0.97– 5.4	0.32–10	0.080
Air–water	0.2–1	0.04–1	0.83–4.2	0.17–4.2	10.6–35.5	0.49–1.64	0.52–5.8	0.047
Air-sugarcane syrup	0.002– 0.2	0.05–1	0.0083–0.83	0.213–4.2	0.03–0.07	10–21	0.035–0.14	0.050
Air-sugarcane syrup (50%)	1	0.2–1	4.2	0.83–4.2	7.2–12	3.03–5.04	2.2–6	0.049

of the interface. In JADIM, the interface location and thickness are both controlled by an accurate algorithm based on Flux-Corrected Transport schemes (Bonometti and Magnaudet 2007).

The equations are discretized on a staggered grid using a finite volume method and all spatial derivatives are approximated using second-order centered schemes. The time scheme used to compute the advective terms in the Navier–Stokes equations is a third-order Runge–Kutta type scheme, while the viscous stresses are solved using a semi-implicit Crank–Nicolson method. The incompressibility is ensured using a projection method, which consists in splitting the velocity field into two contributions: a rotational one, which gives a predicted velocity field calculated semi-implicitely, and a potential one, which is obtained from a pressure correction solution of a pseudo-Poisson equation whose divergence is null.

3.2 Capillarity contribution

3.2.1 Continuum surface force method

The capillary contribution $\mathbf{F}_{\sigma,\mathbf{s}}$ is of main importance in flows controlled by capillarity as is the case in microchannels. The numerical method used to solve the interfacial force is the continuum surface force (CSF) proposed by Brackbill et al. (1992). The localization of the interface is available through a non-zero gradient of volume fraction and the curvature is calculated from the volume fraction gradient. Thus, the surface force $\mathbf{F}_{\sigma,\mathbf{s}}$ is transformed into a volume force $\mathbf{F}_{\sigma,\mathbf{v}}$ by distributing its effects over grid points in the vicinity of the interface in a region of thickness of few cells where $\nabla C \neq 0$:

$$\mathbf{F}_{\sigma,\mathbf{v}} = -\sigma \underbrace{\nabla \cdot \left(\frac{\nabla C}{\|\nabla C\|} \right)}_{\text{curvature}} \underbrace{\nabla C}_{\text{localization/orientation}} \tag{6}$$

The discretization of the capillary force (Eq. 6) is well known to produce artificial vorticity in the vicinity of the interface and unphysical streams called 'spurious currents'. Following the method of Brackbill et al. (1992), a smoothing step on C is introduced to decrease the variations in the curvature and reduce spurious currents.

3.2.2 Characterization of spurious currents

The objective of this section is to characterize the spurious currents for microchannel geometries. The spurious velocities generated by the calculation of the capillary term are measured using two norms as introduced by Renardy and Renardy (2002) and Francois et al. (2006) corresponding to the maximum spurious velocity (l_∞) and the averaged spurious velocities in the domain (l_1), respectively:

$$l_\infty = \max_{i,j,k} \left(\|\mathbf{U}_{\mathbf{i},\mathbf{j},\mathbf{k}}\| \right) \tag{7}$$

$$l_1 = \frac{1}{N_x N_y N_z} \sum_{i,j,k} \|\mathbf{U}_{\mathbf{i},\mathbf{j},\mathbf{k}}\| \tag{8}$$

To characterize the intensity of these spurious currents, a simple configuration has first been analysed (Francois et al. 2006; Dupont and Legendre 2010). A circular drop of radius $R_0 = 1$ mm is placed at equilibrium at the center of a gas domain $l_x \times l_y = 4 \times 4$ mm^2. The computational domain is divided regularly in the x- and y-directions into 96 meshes which corresponds to a uniform spacing in both directions of $\Delta x = \Delta y = l_x/96 \sim 0.042$ mm. The condition imposed at the boundaries is zero velocity and the initial condition on the velocity field is zero. The fluid properties for this test are $\rho_\mathrm{L} = 10^3$ kg/m^3, $\rho_\mathrm{G} = 1$ kg/m^3 for the liquid and gas densities, $\mu_\mathrm{L} = 10^{-2}$ Pa · s, $\mu_\mathrm{G} = 10^{-5}$ Pa · s for the liquid and gas viscosities and $\sigma = 0.072$ N/m for the surface tension.

Secondary tests have been performed for the geometry, fluid properties and boundary conditions corresponding to the microchannel flows considered in this study. Half of a 2D Taylor bubble $l_{\mathrm{B},x} = 0.72$ mm and $l_{\mathrm{B},y} = 0.16$ mm is placed at equilibrium at the center of the domain $l_x \times l_y = 2 \times 0.2$ mm. A regular mesh is used in both directions $n_x \times n_y = 250 \times 50$ that leads to a grid spacing $\Delta x = 8$ µm and $\Delta y = 4$ µm. The conditions imposed at the boundaries are zero velocity on the north face, symmetry on the south face and periodicity on east and west faces. The fluid properties for this test are $\rho_\mathrm{L} = 10^3$ kg/m^3, $\rho_\mathrm{G} = 1.204$ kg/m^3 for the liquid and gas densities, $\mu_\mathrm{L} = 10^{-1}$Pa · s, $\mu_G = 1.815 \times 10^{-5}$Pa · s for the liquid and gas viscosities and $\sigma = 0.07$ N/m for the surface tension.

Table 3 reports the stable spurious velocities obtained after a significant number of iterations for the different test cases. The spurious velocities, based on the norm l_∞, have been found to be proportional to:

$$u_\mathrm{SC} \sim 0.01 \frac{\sigma}{\mu_L} \quad \text{i.e. } Ca_\mathrm{SC} \sim 0.01. \tag{9}$$

This magnitude is comparable to the simulations reported by Lafaurie et al. (1994) ($\sim 0.01\ \sigma/\mu_\mathrm{L}$) and Dupont and Legendre (2010) ($\sim 0.005\ \sigma/\mu_\mathrm{L}$). The spurious velocities thus appear at capillary numbers $Ca_\mathrm{SC} \sim 0.01$ indicating that error-free numerical simulations can only be performed for $Ca > Ca_\mathrm{SC}$.

3.3 Mesh and boundary conditions

Two-dimensional numerical simulations that simulate flow in an infinitely wide channel were performed in a plane 200 µm high to simulate half the height of the microchannel. Every 2D simulation is performed using the same

Table 3 Spurious velocities evaluated from a confined bubble at rest

Test case	l_∞ (m/s)	l_1 (m/s)	σ/μ_L (m/s)	Δt ($\times 10^{-6}$ s)	Iterations
2D circular bubble ($R_0 = l_x/4$)	0.0409	0.000239	7.2	1	20,000
2D long bubble 1 ($l_{B,x}/l_{B,y} = 4.5$)	0.00542	0.000123	0.7	0.25	200,000
2D long bubble 1	0.00702	0.000162	1.4	0.20	250,000
2D long bubble 1	0.00353	0.0000983	0.35	0.25	200,000
2D long bubble 2 ($l_{B,x}/l_{B,y} = 12$)	0.00459	0.000969	0.7	0.25	200,000

boundary conditions and the same fluid properties that were used to characterize the spurious currents. A pressure gradient is imposed between the two periodic boundaries to generate fluid flow. Two domains of simulation have been used: a short one (Domain 1: $l_x = 2$ mm) that allows bubble lengths about 1 mm to be simulated and a longer one (Domain 2: $l_x = 5$ mm) for the simulation of bubbles that are a few millimeters long. For each domain, simulations have been performed by varying the volume fraction of air at the initialization stage and by varying the pressure gradient across the domain.

Domain 1 is the computational domain described in the spurious currents characterization section and comprises 12,500 nodes. Since there were only about five grid cells in the liquid film, which is the lower limit for the correct simulation of the film (Gupta et al. 2009), the convergence has been tested with a second, finer mesh. This second grid is coarser in the bubble region and finer in the liquid film area compared with the first mesh, however, the total number of nodes (12,500) remained unchanged. This refined mesh consists in a uniform grid spacing along the channel ($n_x = 250, \Delta x = 8$ μm) and a non-uniform grid spacing across the width of the channel: $n_y = 50$ with a regular spacing for $y < 115$ μm (16 nodes) and irregular mesh with a factor 0.92 for 115 μm $< y$ (34 nodes). Thus, the grid spacing across the channel width varies between $\Delta y_{max} = 7.20$ μm and $\Delta y_{min} = 0.46$ μm. The simulations with both grids converged to the same velocity field, however, the number of iterations needed to converge is almost 20 times greater for the non-uniform mesh than for the regular mesh. The regular mesh is, therefore, considered adequate for the simulation of these flows and allows a much larger time step than the non-uniform mesh does. Domain 2 is meshed in the same way as domain 1, such that there are at least 5 grid cells in the liquid film and a regular mesh is used in both directions $n_x \times n_y = 500 \times 40$ (i.e. 20,000 nodes), which leads to a grid spacing $\Delta x = 10$ μm and $\Delta y = 5$ μm.

4 Results and discussion

Figure 3a summarises the numerical and physical experiments performed in this study to characterize the bubble lengths, shapes and velocities of gas–liquid Taylor flow in rectangular microchannels as a function of the Reynolds and capillary numbers. The numerical simulations were carried out with fluid properties such that the spurious velocities were lower than the physical velocities of the flow.

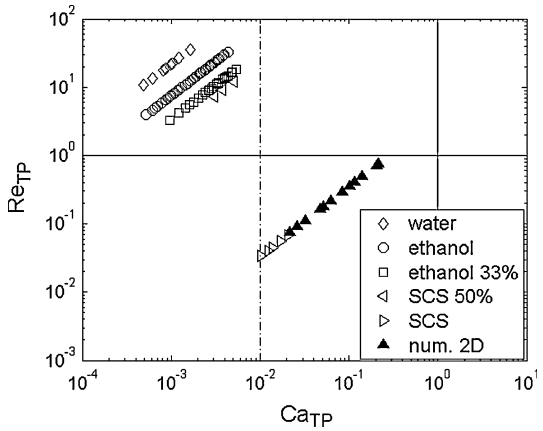

Fig. 3 Reynolds and capillary numbers of the experiments and numerical simulations performed. *Dash dot dash line* minimum capillary number available numerically to neglect spurious currents

4.1 Bubble generation

Figure 4 shows the bubble generation mechanism for the ethanol-air system. This mechanism can be divided into several steps: (a to b) the bubble starts growing in the side channel, perpendicularly to the direction of the liquid flow in the main channel; (b to d) as the bubble grows, the gas–liquid interface is distorted by the liquid in main channel and the radius of curvature upstream of the leading bubble cap increases; (d) during this time, the interface detaches from the upstream wall of the gas inlet and the contact line starts moving into the gas inlet; (d to e) the air fills the main channel and the bubble occupies the width of the main channel; (e to f) the gas–liquid interface coming from the gas inlet is pushed downstream until pinching off occurs and the bubble is formed.

In the majority of ethanol-air experiments, bubbles are pinched off at the T-junction and regular bubble trains are observed, as shown in Fig. 4. For these experiments, the

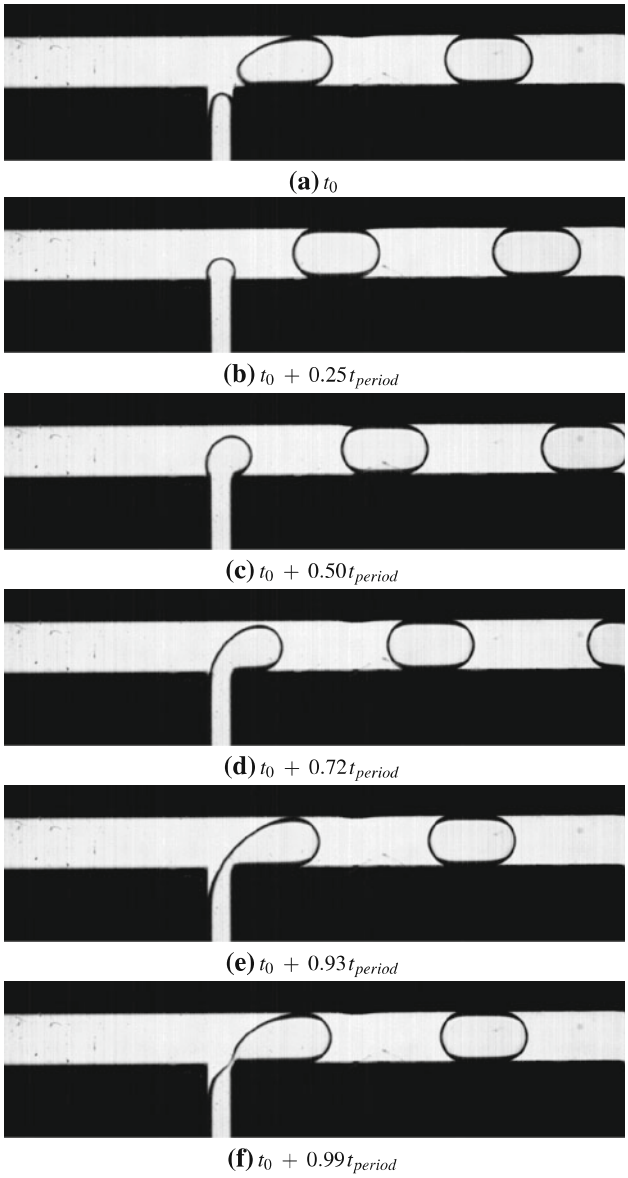

Fig. 4 Bubble generation in air–ethanol flows. $U_L = 0.021$ m/s and $U_G = 0.0105$ m/s, evolution of Taylor flow during a period where bubbles are generated every $t_{period} = 0.125$ s, i.e. with a frequency of formation about 8 Hz

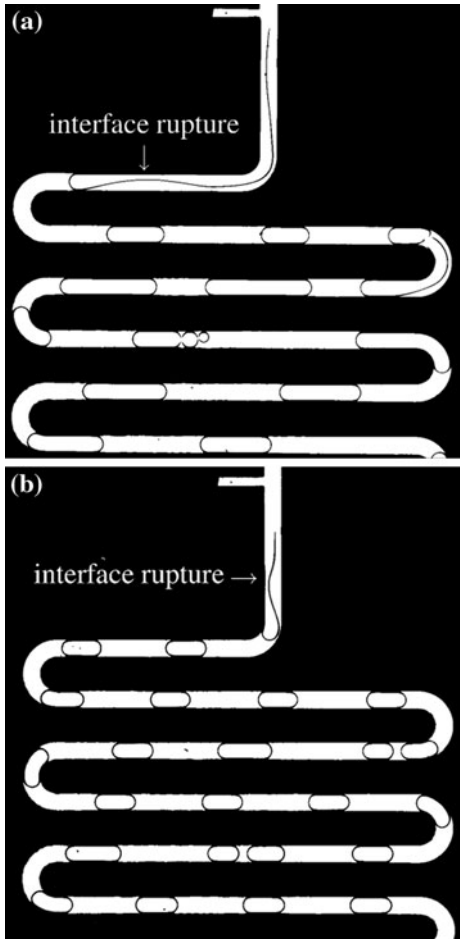

Fig. 5 Bubble generation and interface rupture in the main channel with **a** air–water system $U_L = 0.021$ m/s and $U_G = 0.0105$ m/s, bubble pinch-off occurs at the gas inlet every $t_{period} = 1.16$ s, i.e. with a frequency about 0.86 Hz; **b** air-sugarcane syrup system, $U_L = 0.042$ m/s and $U_G = 0.021$ m/s bubble pinch-off occurs at the gas inlet every $t_{period} = 0.97$ s, i.e. with a frequency about 1 Hz

standard deviation of the average bubble size is less than 5 %. In general, the fluctuations in the bubble velocities are only about 1–2% of the average value. Fig. 5 shows the generation of air bubbles in water and sugarcane syrup. For both the air–water and air-sugarcane syrup systems, an iterative break-up mechanism is observed. For the most part, the bubble generation occurs in the main channel, well after the T-junction. However, after the generation of several bubbles in the main channel far from the T-junction, a bubble is then pinched off at the T-junction before bubble break-up occurs in the main channel again. It is interesting to point out that for air-sugarcane syrup, this break-up mechanism results in a rather periodic structure, which is not so obvious with the air–water system. Nevertheless, for both the water and sugarcane syrup systems, these flows result in irregular bubble lengths with a standard deviation greater than 10% of the average length. Once the bubble train is established, the bubble velocities are constant. Similar irregular flows were also found to occur with ethanol/water solutions at low liquid flow rates.

We distinguish these two processes of bubble generation by naming the regular bubble flow as the squeezing regime (Garstecki et al. 2006) and the irregular bubble flow (with bubble generation in the main channel) as the leakage regime. The leakage regime described here looks similar to the parallel liquid–liquid flow that breaks in the microchannel to form droplets as observed by Guillot and Colin (2005). However, the flow conditions required for the transition between the squeezing regime and unstable parallel flow pinching in the channel remain unclear.

According to Akbar et al.'s (2003) criteria, bubble or slug flow is expected for all of the flow conditions studied here. However, the unstable leakage regime is observed for both viscous liquids (i.e. sugarcane syrup solutions), as well as low viscosity liquids (i.e. water). It is, therefore, thought that the wettability of the microchannel material by the liquids also plays an important role in the bubble generation process.

In addition, for equal gas and liquid flow rates, a decrease in the frequency of bubble formation was observed with air-diluted ethanol system when compared with the pure ethanol system. However, in both cases the bubble nose and rear are the same shape, which is in agreement with the corresponding values of the capillary and Weber numbers; under these conditions, the stabilizing effect of the capillary force is dominant and minimizes the bubble surface.

4.2 Bubble and slug lengths

Figure 6 shows the evolution of the dimensionless bubble lengths as a function of the Weber number for the air–ethanol systems. For a fixed flow rate ratio U_G/U_L, the bubble and slug lengths decrease slightly when the superficial two-phase velocity increases. This decrease in bubble and slug size can be explained by the increase in energy input to the system; similar observations have been made for drop formation in micromixers (Haverkamp et al. 1999). Thus, for a given gas hold-up, the frequency of bubble formation $f \sim U_B/(L_B + L_S)$ increases with inertia. Similar phenomena are observed for other fluid pairs, however, for fixed flow conditions, the bubble/slug period is shorter with ethanol than it is with the ethanol solution (33%), which is shorter than the bubble/slug periods for water alone. This is primarily due to the higher surface tension of water compared with ethanol.

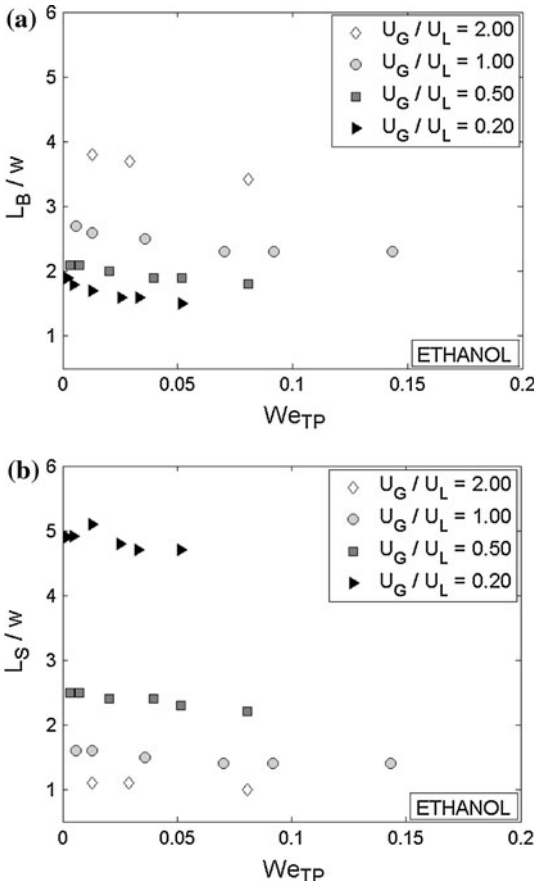

Fig. 6 Bubble and slug lengths versus the Weber number We_{TP} in air–ethanol system for volumetric flow rate ratios $U_G/U_L = [2;\ 1;\ 0.5;\ 0.2]$

Figure 7 shows the evolution of dimensionless bubble and slug lengths as a function of the flow rate ratios for different fluid pairs. The experiments were conducted by varying the gas flow rate at a fixed liquid flow rate ($U_L = 0.021$ m/s). For each fluid system, the bubble and slug lengths increase linearly with the gas-to-liquid and liquid-to-gas velocity ratios, respectively. It can be seen that the bubble and slug lengths are greater with water than they are with ethanol for the same flow rate conditions. Again, this shows that for a fixed flow rate ratio, the bubble and slug lengths decrease and the frequency of bubble break-up increases when the Weber number increases. It should be pointed out that for the results presented in Fig. 7a,b, the flow for the ethanol and diluted ethanol (33%) systems was regular and bubbles were formed via the squeezing mechanism, whilst the air–water flow was irregular (as suggested by the error bars) with bubble formation in the main channel (leakage regime).

The linear evolution of the bubble and slug lengths with the flow rate ratios is in agreement with the model proposed by Garstecki et al. (2006) for the estimation of drop and bubble lengths. According to the Garstecki model, the lengths of bubbles (and drops) generated in side-entering T-junction microchannels with rectangular cross-section can be determined from the continuous and dispersed phase flow rates. The model was developed using data obtained in microchannels with characteristic dimensions on the order of 100 μm at low capillary ($Ca_{TP} < 10^{-2}$) and Reynolds numbers ($Re_{TP} < 1$). Under these conditions, the effects of shear stress dominate the inertial effects and both are negligible compared with the interfacial stresses and pressure gradients. Garstecki et al. (2006) postulate that the dynamics of drop and bubble break-up is dominated by the pressure balance between the dispersed and continuous phases due to the interfacial stresses and the pressure drop generated by the resistance of the flow induced by the bubble or drop. The authors identified four stages of the break-up process for their model: (1) the tip of the bubble enters the main channel, (2) the filling stage where the

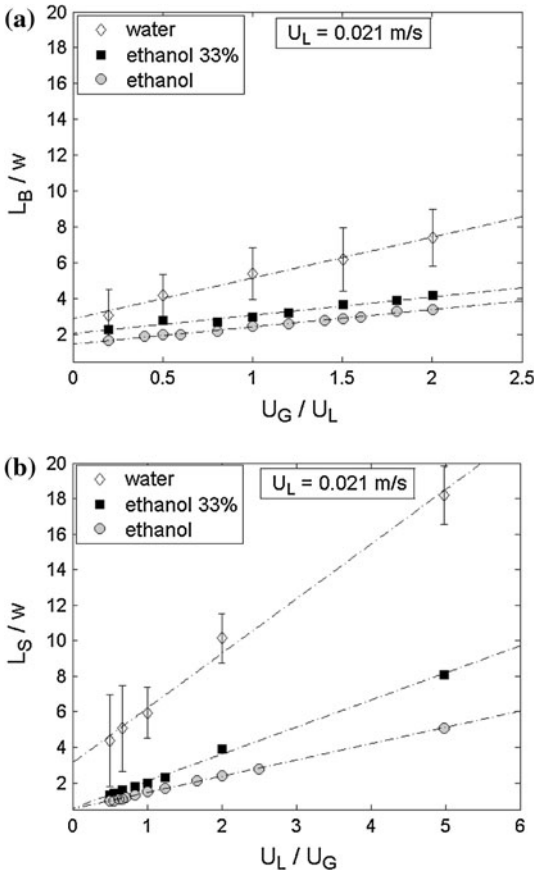

Fig. 7 **a** Dimensionless bubble lengths and **b** dimensionless slug lengths for varying gas phase velocities and a fixed liquid phase velocity $U_L = 0.021$ m/s for water, $We_L = 0.43$ (*open diamond*); diluted ethanol (33%), $We_L = 0.30$ (*open square*); and ethanol, $We_L = 0.18$ (*open circle*). *Error bars* represent the standard deviation for the water-air system; the standard deviation on bubble and slug lengths for the ethanol and the diluted ethanol (33%) systems was negligible with this liquid velocity. *Dash dot dash line* experimental fitting

bubble occupies almost all the cross-section, (3) the squeezing stage where the radius of curvature of the interface increases and the interface at the gas inlet is squeezed, (4) the break-up stage where the Laplace pressure reaches a maximum as the radius of curvature tends to infinity and the discontinuous phase pinches off. Following this, they suggest that the bubble or drop generation process can be divided into two main steps and that the time for bubble or drop formation t_{growth} is the sum of the filling and squeezing times. The scaling relation they proposed is $t_{growth} = t_{filling} + t_{squeezing}$ where $t_{growth} = L_B/u_{growth}$, $t_{filling} = w/u_{filling}$ and $t_{squeezing} = d_{neck}/u_{squeezing}$, where d_{neck} is the characteristic dimension of the neck of the bubble at the beginning of the squeezing stage. If the filling and squeezing stages are independent, it can be assumed that $d_{neck} \sim w_{in}$. The characteristic velocities of the different stages can be expressed as a function of the dispersed and continuous phase flow rates: $u_{growth} = Q_G/A_{ch}$, $u_{filling} = Q_G/A_{ch}$ and $u_{squeezing} = Q_L/A_{ch}$. Accordingly, the bubble length is given by:

$$\frac{L_B}{w} \sim 1 + \frac{w_{in}}{w}\frac{Q_G}{Q_L}. \tag{10}$$

However, in microchannels of rectangular cross-section, liquid flows around the dispersed phase during the squeezing stage thereby increasing the squeezing time. Van Steijn et al. (2007) improved the Garstecki model by taking this leakage flow into account and estimated the bubble length as:

$$\frac{L_B}{w} = \lambda_1 + \lambda_2 \frac{U_G}{U_L}, \tag{11}$$

where $\lambda_1 = 1.5$ and $\lambda_2 = 1.5\ w_{in}/w$. Völkel (2009) suggested that the length of the liquid slug should follow a scaling law similar to the gas phase:

$$\frac{L_S}{w} = \lambda_2 + \lambda_1 \frac{U_L}{U_G}. \tag{12}$$

Pohorecki and Kula (2008) also proposed a 'switching' mechanism to predict bubble lengths in Y-junction microchannels and presented a simple model: $L_B/w \sim \varepsilon_L^{-1}$, i.e. $L_B/w \sim 1 + U_G/U_L$. This model is almost identical to that proposed by Garstecki et al. (2006) with the difference that the gas-to-liquid inlet width ratio is not explicitly taken into account since the gas and liquid inlets used by Pohorecki and Kula (2008) were the same size. It is interesting to note that their experimental results, which were obtained in microchannels of square and circular cross sections as well as different materials, agree relatively well with this model. It is interesting to note that according to both Garstecki et al.'s (2006) and Pohorecki and Kula's (2008) models, the bubble lengths only depend on the continuous and dispersed phase flow rates and the microchannel dimensions; there appears to be no dependency on the physical properties of the fluids. Recently, Leclerc et al. (2010) also proposed a unique scaling law for bubble generation in various T-junction geometries. Again, it enables bubble lengths to be predicted from flow rates and microchannel dimensions only. It should be pointed out, however, that the effects of fluid and material properties on bubble generation were not investigated.

The results in Fig. 7 show that when $U_G \ll U_L$, the minimum bubble length is greater than the width of the microchannel w and appears to depend on the liquid phase properties. In fact, as shown in Fig. 4, the squeezing stage can start even if the bubble is not completely filling the cross-section area, which results in bubble lengths $L_B > w$. In this case, it appears that the same scaling relation can still be applied, however, the coefficients λ_1 and λ_2 may be

slightly different to the values found by van Steijn et al. (2007). It can also be pointed out that although Garstecki et al. (2006) presented their model for the estimation of both drop and bubble lengths, it only correctly estimates bubble lengths under certain operating conditions. In fact, although the bubble/drop generation process is apparently independent of fluid properties (i.e. viscosity, density and surface tension) under the conditions studied by Garstecki et al. (2006), a close inspection of their results suggests that other properties of the carrier liquid (e.g. wettability) play a non-negligible role in the generation process. As a result, it is not clear that all fluid pairs follow a single scaling law.

It also can be seen in Fig. 7 that the length of the liquid slug increases with U_L/U_G, as suggested by Völkel (2009). However, the coefficients λ_1 and λ_2 appear to depend on both the fluid properties and the liquid velocity, and do not appear to have the same value as the coefficients of Eq. (11). Indeed, the coefficients for ethanol are close to 1.5 in the squeezing regime but they appear to increase when the break-up mechanism changes and tends towards the leakage regime (Figs. 7, 8).

Qian and Lawal (2006) carried out 2D simulations of the break-up of Taylor bubbles in T-junctions and side-entering T-junctions. They proposed a correlation for the prediction of bubble lengths ($L_B/w = 1.637\varepsilon_G^{0.107}(1-\varepsilon_G)^{-1.05}Re_{TP}^{-0.075}Ca_{TP}^{-0.0687}$), which underlines the predominant contribution of the flow rate ratio and only a slight effect of surface tension and viscosity. Although a few points remain unclear in Qian and Lawal's (2006) study - they used a coarse grid that was inadequate to correctly detect the liquid film and no details on the surface tension conditions that determine bubble break-up - it is interesting to point out that the bubble lengths obtained in this study for the air–ethanol systems at various Weber numbers (Fig. 6) agree with the Qian and Lawal (2006) correlation. However, when water or sugarcane syrup are used as the carrier fluid, the squeezing mechanism does not occur. Instead, parallel flow develops before bubble generation occurs in the main channel and in this case the data do not agree with the Qian and Lawal (2006) correlation. Indeed, the dependency of the bubble lengths on the fluid properties has shown to be much more significant here than ever shown in previous studies. The transition from the squeezing regime to the leakage regime is difficult to detect based solely on the competition of capillary, viscous and inertial effects; it is thought that the wettability of microchannel by the liquid really plays a non-negligible role.

Figure 8 shows the evolution of the bubble and slug lengths as a function of the the flow rate ratios for the air-diluted ethanol (33%) system at fixed superficial liquid velocities. This figure highlights the linear evolution of the

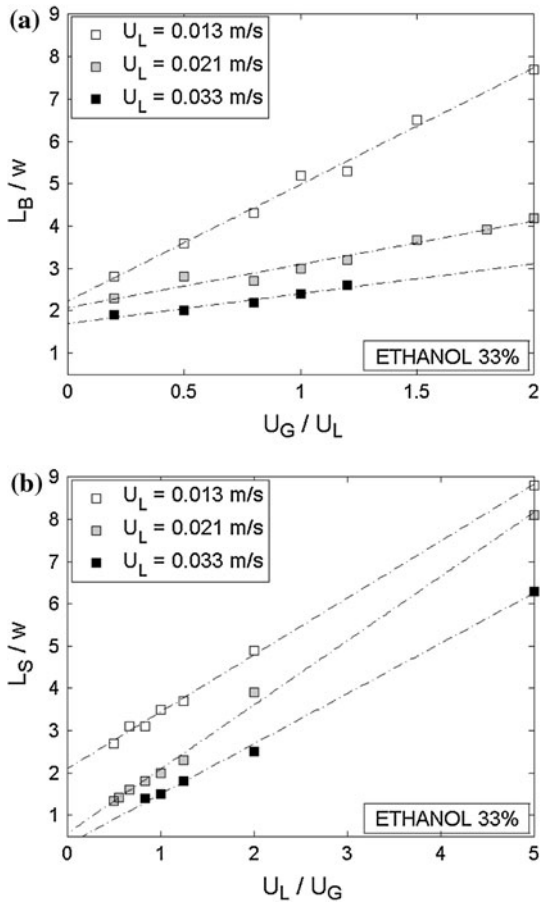

Fig. 8 Bubble and slug lengths versus ratio of air and liquid velocities U_G/U_L (**a**), and U_L/U_G (**b**) in ethanol 33%/air system for given liquid velocities: $U_L = [0.008;\ 0.021;\ 0.042]$ m/s. *Dash dot dash line* experimental fitting

bubble and slug lengths with the gas-to-liquid and liquid-to-gas velocity ratios respectively, which is in agreement with Eqs. (11) and (12). The coefficients λ_1 and λ_2 of the linear scaling law for this fluid pair decrease when the liquid velocity increases. It was observed that regular bubble sizes were generated at a high frequency with high liquid flow rates, whereas a decrease in the liquid flow rate leads to irregular flows of longer bubbles and slugs at a lower frequency. This transition from squeezing to leakage regime is also visible with water for which a similar linear evolution is also found. However, for the pure air–ethanol experiments, where the bubble generation was generally very regular, the bubble and slug lengths are not so dependent on the liquid velocities. Figure 8 also shows that for a fixed gas fraction, the bubble lengths decrease as the liquid velocity increases and the energy input into the system increases. Thus, the bubble and slug lengths, as well as the frequency of bubble generation, appear to be governed mainly by the competition between gas and liquid velocities, as well as the competition between inertial and capillary effects.

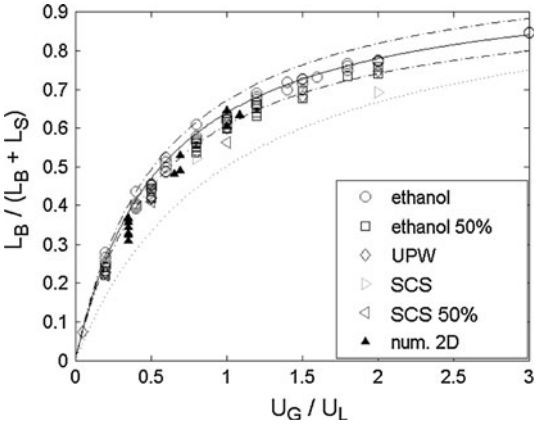

Fig. 9 Dimensionless bubble length versus ratio air/liquid flow rates. *Dotted line* relative bubble length in the case of a zero liquid film thickness. *Straight line* Experimental fitting from averaged values of coefficients λ_1 and λ_2 using the van Steijn representation (Eq. 11). *Dash dot dash line* deviation of 5% from the experimental fitting

Interestingly, when the bubble length relative to the total length of a bubble/slug unit is plotted as a function of the flow rate ratio, as shown in Fig. 9, the squeezing and leakage regimes observed seem to collapse; slight differences can be accounted for by the varying effects of capillarity, inertia and viscosity. This suggests that the relative quantity of liquid surrounding the bubble (in the liquid film and around the caps) is almost the same for the different fluid pairs at a given gas hold-up, whatever the bubble break-up frequency.

The difference between the experimental points and the curve for the relative bubble length in the case of zero liquid film shows that the quantity of liquid surrounding the bubble increases with U_G/U_L, reaches a maximum around $U_G/U_L = 1$ and then decreases slightly. Results from numerical simulations are also reported in this figure and their agreement with the experimental data is good despite their 2D nature.

4.3 Liquid film

The liquid film between the bubble and the microchannel wall has been evaluated with 2D simulations. This 2D representation is a simplified approach to the problem and does not take into account the liquid film in the corners of the channel. However, de Lózar et al. (2008) have shown that the liquid flow from the film to the corners is weak and does not significantly deform the gas–liquid interface. Although the 2D simulations do not provide detailed information on the varying liquid film thickness around the bubble and the 3D bubble shape, they nevertheless provide a useful information. The qualitative trends observed in 2D representation are expected to be similar to 3D cases. Indeed, Sarrazin et al. (2006) studied velocity field and mixing in liquid–liquid microsystems and they observed similar hydrodynamic flow structures in 2D and 3D rectangular cases (with an aspect ratio close to unity). Furthermore, the information obtained through these 2D simulations is also expected to be valid for high aspect ratio rectangular microchannels. In the following, the liquid film hold-up around a Taylor bubble is considered and defined as $\varepsilon_L = A_L/A_{ch}$ where A_L is the area occupied by the liquid. In the literature, the bubble velocity is often related to this liquid film hold-up (see Völkel 2009 for an overview). Under several conditions, such as constant surface tension and a flat annular liquid film, there is no pressure gradient along the bubble and the velocity in the liquid film is assumed to be zero. Thus, using the mass conservation relationship, the bubble velocity can be related to the liquid film hold-up and the two-phase velocity: $U_B/U_{TP} = 1/(1-\varepsilon_L)$.

Since the liquid film hold-up is typically very low in Taylor flow, the bubble velocities can be expected to be close to the sum of the gas and liquid superficial velocities. Although the linear plots of the bubble lengths given in Figs. 7 and 8 suggest information on the leakage flow around the bubble at the T-junction contacting section, the measurement of the liquid film thickness around Taylor bubbles is not straightforward experimentally. However, it can be quite easily obtained with correctly performed numerical simulations. Figure 10a shows the dimensionless liquid film thickness around the Taylor bubble obtained numerically as a function of the capillary number based on the bubble velocity, as suggested in the first studies of Taylor (1961) and Bretherton (1961). In this latter work, a correlation assuming the 'lubrication approximation' is proposed for the determination of the liquid film thickness from the capillary number in tubes or 2D planar geometries. This correlation is valid for flows where $Ca_B \ll 1$ and the inertial effects are negligible compared with the surface tension and viscous effects: $\delta/r_h = 1.34\ Ca_B^{2/3}$, where δ is the liquid film thickness, r_h is the hydraulic radius and Ca_B is the Taylor bubble capillary number based on the bubble velocity.

Aussillous and Quéré (2000) extended Bretherton's (1961) correlation to high capillary numbers in capillary tubes:

$$\frac{\delta}{r_h} = \frac{1.34 Ca_B^{2/3}}{1 + k \times 1.34 Ca_B^{2/3}}. \quad (13)$$

The coefficient 1.34 was derived by Bretherton (1961) and the coefficient $k = 2.5$ was found empirically (Aussillous and Quéré 2000). Thus, the liquid film thickness tends toward a maximum value of 1/2.5 $\sim$ 0.4 as the capillary number increases.

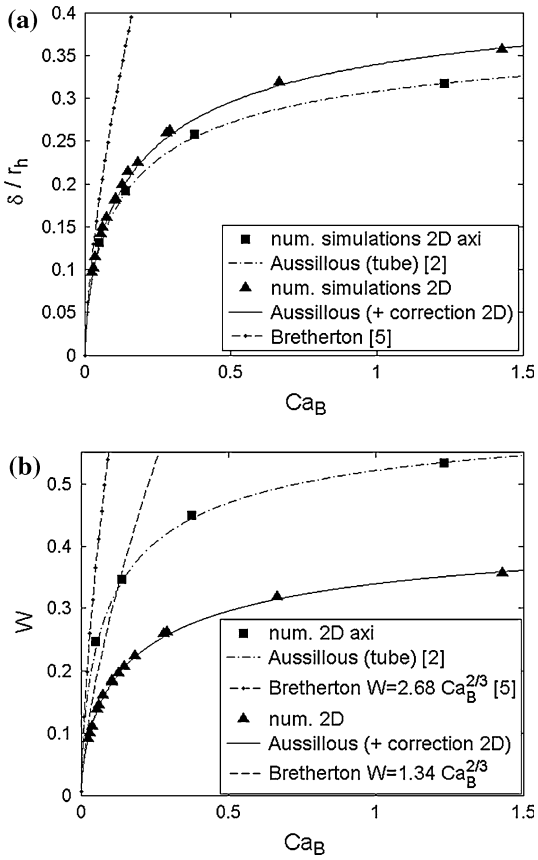

Fig. 10 **a** Dimensionless liquid film thickness determined from numerical simulations as a function of the capillary number. **b** Dimensionless bubble velocities $W = (U_B - U_{TP})/U_B$ versus the capillary number

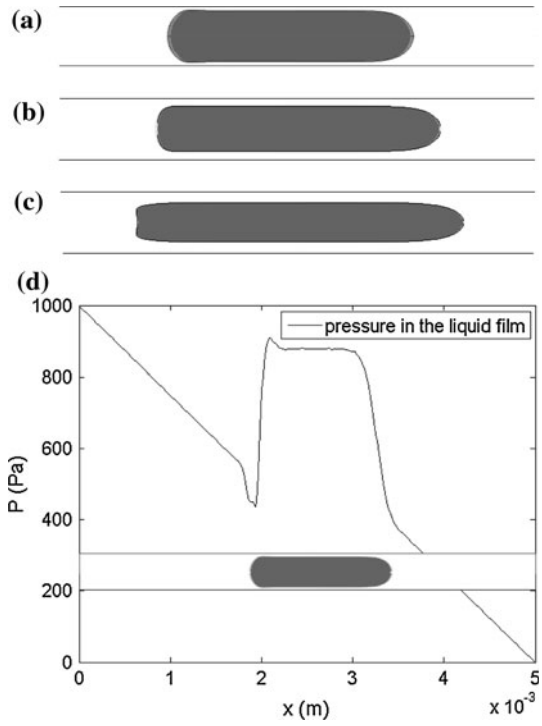

Fig. 11 Bubbles shapes obtained numerically under different conditions: **a** $Ca_B = 0.055$, **b** $Ca_B = 0.293$, **c** $Ca_B = 1.47$, gas hold-up is fixed $\alpha_G \sim 0.25$. **d** pressure field in the liquid film corresponding to case (**a**): P decreases linearly from $P_0 + 1000$ (Pa), capillary pressure jump, P remains constant along the bulk of the bubble, capillary pressure jump, P decreases linearly to P_0. Domain: $l_x \times l_y = 5 \times 0.2$ mm. *Blue* air, *red* liquid; the interface is distributed over about 3–4 meshes at the maximum elongation (tail and nose)

In Fig. 10a, it can be seen that the liquid film thickness obtained by the 2D axisymmetrical simulations is correctly described by Eq. (13). In the 2D geometry, the liquid film thickness increases with increasing capillary number, however the asymptotic value at large capillary numbers is higher than that obtained in tubes (1./2.2 $\sim$ 0.455). Therefore, an equation similar to Eq. (13) can be proposed for 2D geometries, whereby the coefficient $k = 2.2$. This equation, with corresponding coefficient k, shows that Bretherton's (1961) correlation is found as the asymptotic behaviour for low capillary numbers, while at higher capillary numbers the liquid film thickness tends towards a maximum value depending on the geometry. In square and rectangular microchannels, the film thickness around the bubble body varies due to the presence of the channel corners (Han and Shikazono 2009b; Hazel and Heil 2002; Liu and Wang 2008; Taha and Cui 2006; Wong et al. 1995). However, although the 3D aspects of the bubble shapes are not considered in these 2D simulations, the asymptotic behaviour of the liquid film is expected to be the same and particularly in channels with a high aspect ratio (i.e. wide shallow microchannels) where the shear rate along the channel width is negligible compared with the shear rate along the depth of the channel. These results are in very good agreement with the theory and allow bubble shapes to be roughly estimated so that the mesh for 3D simulations, which are much more computationally expensive, can be adapted to correctly capture the liquid film in Taylor flow.

In addition to the increase in the liquid film thickness, a flattening of the rear of the bubble and an elongation of the nose of the bubble can be seen with increasing capillary number in the simulated results as shown in Fig. 11a–c. Such a loss of symmetry was also observed in the experiments with sugarcane syrup solutions where the capillary number is of the order of 10^{-2} and the liquid film is visibly thick. Figure 11d shows the pressure field in the liquid film and there is indeed no pressure gradient along the bulk of the bubble, which statisfies the hypothesis of the stagnant film.

The changes in the shape of the bubbles rear and nose have also been observed in several other studies, including planar cases (Giavedoni and Saita 1997), circular

capillaries (Fouilland et al. 2010; Gupta et al. 2009; Triplett et al. 1999) and square channels (Liu and Wang 2008; Taha and Cui 2006). This phenomenon can be understood from the pressure drop across the bubble caps. In Bretherton's work (1961), the asymptotic behaviour of the pressure drop at vanishing Ca was studied. It was found that the pressure drop at the front cap of an axisymmetrical bubble is $\Delta p_{\text{front}} = \frac{2\sigma}{r_h}\left(1 + 3.72 Ca_B^{2/3}\right)$ and the pressure drop at the rear cap is $\Delta p_{\text{rear}} = \frac{2\sigma}{r_h}\left(1 - 0.97 Ca_B^{2/3}\right)$. From these relationships, it can be seen that the pressure drop at the front cap increases with the capillary number while it decreases at the rear cap. Even if this asymptotic behaviour can not be used at higher capillary numbers ($Ca_B > 10^{-2}$), Giavedoni and Saita (1997) and Hazel and Heil (2002) found similar trends in 2D and rectangular channels, respectively, where the pressure drop across the front tip of the bubble increases with Ca_B.

4.4 Bubble velocities

Since the liquid film thickness obtained by the numerical simulations in the visco-capillary regime is correctly described by Eq. (13), the dimensionless bubble velocity W can be deduced as the following, respecting the stagnant film hypothesis:

$$W = \frac{U_B - U_{TP}}{U_B} = 1 - \left(1 - \frac{\delta}{r_h}\right)^m, \tag{14}$$

where $m = 1$ for 2D cases and $m = 2$ for tubes. Figure 10b shows that both the 2D and axisymmetrical simulations are in good agreement with the scaling laws obtained from the liquid film thickness. The relationship for the evaluation of bubble velocity, as first proposed by Bretherton (1961), is also found at low capillary numbers ($Ca_B < 0.01$) where the liquid film is very thin: $W = m \times 1.34\ Ca_B^{2/3}$.

In this work, the experiments were performed for a range of low capillary numbers ($Ca_B < 0.01$) and moderate Reynolds numbers ($1 < Re_B < 100$). Under these conditions, the effects of inertia are not negligible compared with our numerical simulations and the conditions studied by Aussillous and Quéré (2000), which were both carried out in the visco-capillary regimes ($Ca_B > 0.01$ and $Re_B < 1$). Since the Weber numbers of the experiments in this study are much larger than those of the simulations and a simple model like relation (13) is not applicable to such conditions, the bubble velocity has been plotted versus the two-phase superficial velocities. Figure 12a shows a linear increase in the experimental bubble velocities with increasing two-phase superficial velocity for the air–ethanol system. This means that the liquid film is of more or less constant thickness along the bubble body in our experiments, which is in

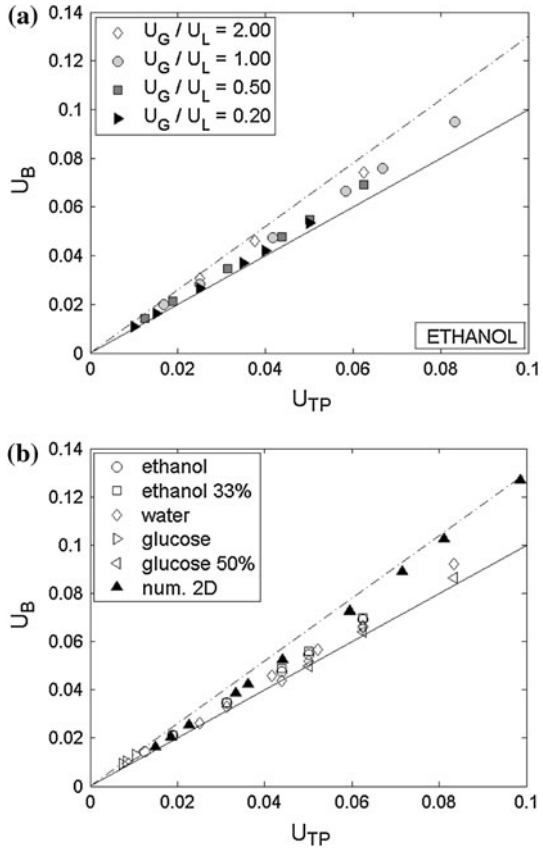

Fig. 12 **a** Bubble velocity versus two-phase velocity for ethanol. **b** Bubble velocity versus two-sphase velocity. *Straight line* $U_B = U_{TP}$ and *Dash dot dash line* $U_B = 1.3 \times U_{TP}$

agreement with the results of Taha and Cui (2006) in square capillaries at low capillary numbers ($Ca_B \ll 1$). The ratio of the bubble velocity to the two-phase velocity is slightly greater than unity, which is coherent with the stagnant film hypothesis and suggests a thin liquid film. Similar results about bubble velocities were reported in Yun et al.'s (2010) study. Indeed, the liquid film between the bubble and the microchannel walls in these experiments was indistinguishable. Figure 12b shows a similar graph, which combines all of the bubble velocities measured experimentally with those obtained by the 2D simulations. The results of the 2D numerical simulations appear to agree relatively well with the experiments, although the bubble velocities increase slightly faster than experimental bubble velocities. In addition to the fact that different effects dominate in the experiments and the numerical simulations, this discrepancy is certainly due to the fact that the lateral walls of the microchannel were not taken into account in the simulations. Indeed, the lateral walls contribute to an increase in flow resistance and dissipation, which results in a reduction of the bubble velocity. 3D simulations are, therefore, necessary for a more accurate comparison with the experiments.

It can also be pointed out that although the cross-sectional area occupied by the liquid film should increase with increasing capillary number (Bretherton 1961; Aussillous and Quéré 2000), the capillary numbers in the experiments were typically very low ($Ca_B < 0.01$) and, therefore, the bubble velocity should be approximately equal to the two-phase superficial velocity. However, inertia is assumed to be negligible in Bretherton's (1961) and Aussillous and Quéré's (2000) works, which is not the case in our experiments at moderate Reynolds numbers. It is, therefore, possible that the Weber number has some effect on the liquid film thickness and thus, the dimensionless bubble velocity. This was also mentioned by Aussillous and Quéré (2000) for conditions in the visco-inertial regimes. Even if the effective dependency of the liquid film thickness or bubble velocity upon the Weber number is not clear at present, these results highlight its possible effects on the hydrodynamics of Taylor bubbles in capillary-inertial regimes.

5 Conclusions

This study has focused on the generation and characteristics of gas–liquid Taylor flow formed in T-junction microchannels. Visualisation experiments using a high speed camera and 2D Volume of Fluid simulations have been performed to study the effects of fluid properties and flow conditions on bubble and slug lengths, liquid film hold-up and bubble velocities. As earlier described by Garstecki et al. (2006) and then by van Steijn et al. (2007), the bubble generation process can be partitioned into several steps and the bubble and slug lengths are a function of the gas and liquid flow rates and independent of fluid properties such as the viscosity and surface tension. This study shows however that a single scaling law for all gas–liquid flows generated in the T-junction is not always possible. The bubble and slug lengths are shown not to depend solely on the gas and liquid flow rates and suggest that the liquid properties (such as wettability) and velocities are also important under certain conditions. This work highlights the effects of the competition between inertial forces and capillarity on the leakage flow and thus on the bubble break-up frequency, which have been negligible in previous studies in the literature due to the low Reynolds numbers employed. Indeed, increasing the inertia of the fluid system results in increased leakage flow and consequently to a decreased frequency of bubble formation. Bubble and slug lengths are, therefore, increased. The results of numerical simulations were found to be in relatively good agreement with the experiments despite their 2D nature. They allow the dimensionless bubble lengths to be predicted relatively well and provide a good estimation of the liquid film thickness in the case of high aspect ratio microchannels, which is difficult to measure experimentally. Furthermore, the 2D simulations allow the stagnant film hypothesis used in modelling to be confirmed. 3D simulations are underway, however, these are very computationally expensive. They will allow a more accurate comparison with the experimental results since the effect of the lateral wall of the microchannel is suspected to contribute to the bubble dynamics. They will also provide more detailed information on the liquid film thickness around the bubbles.

Acknowledgments This work was financed by the French "Agence Nationale de la Recherche" in the framework of the project MIGALI no. ANR-09-BLAN-0381-01. We also acknowledge the support for this project from the CNRS research federation FERMaT, such as the CALMIP project for providing computational resources.

References

Akbar MK, Plummer DA, Ghiaasiaan SM (2003) On gas–liquid two-phase flow regimes in microchannels. Int J Multiph Flow 29:855–865

Aussillous P, Quéré D (2000) Quick deposition of a fluid on the wall of a tube. Phys Fluids 12(10):2367

Bonometti T, Magnaudet J (2007) An interface-capturing method for incompressible two-phase flows. Validation and application to bubble dynamics. Int J Multiph Flow 33:109–133

Brackbill J, Kothe DB, Zemach C (1992) A continuum method for modeling surface tension. J Comput Phys 100:335–354

Bretherton FP (1961) The motion of long bubbles in tubes. J Fluid Mech 10:166

de Lózar A, Juel A, Hazel AL (2008) The steady propagation of an air finger into a rectangular tube. J Fluid Mech 614:173–195

De Menech M, Garstecki P, Jousse F, Stone HA (2008) Transition from squeezing to dripping in a microfluidic T-shaped junction. J Fluid Mech 595:141–161

Dupont J-B, Legendre D (2010) Numerical simulation of static and sliding drop with contact angle hysteresis. J Comput Phys 229:2453–2478

Fouilland TS, Fletcher DF, Haynes BS (2010) Film and slug behaviour in intermittent slugannular microchannel flows. Chem Eng Sci 65:5344–5355

Francois MM, Cummins SJ, Dendy ED, Kothe DB, Sicilian JM, Williams MW (2006) A balanced-force algorithm for continuous and sharp interfacial surface tension models within a volume tracking framework. J Comput Phys 213:141–173

Garstecki P, Fuerstman MJ, Stone HA, Whitesides GM (2006) Formation of droplets and bubbles in a microfluidic T-junction—scaling and mechanism of break-up. Lab chip 6:437–446

Giavedoni MD, Saita FA (1997) The axisymmetric and plane cases of a gas phase steadily displacing a Newtonian liquid—a simultaneous solution of the governing equations. Phys Fluids 9(8):2428

Guillot P, Colin A (2005) Stability of parallel flows in a microchannel after a T junction. Phys Rev E 72:066301

Gupta A, Kumar R (2010) effect of geometry on droplet formation in the squeezing regime in a microfluidics T-junction. Microfluid Nanofluid 8:799–812

Gupta R, Fletcher DF, Haynes BS (2009) On the CFD modelling of Taylor flow in microchannels. Chem Eng Sci 64:2941–2950

Gupta R, Fletcher DF, Haynes BS (2010) CFD modelling of heat and mass transfer in the Taylor flow regime. Chem Eng Sci 65:2094–2107

Han Y, Shikazono N (2009a) Measurement of the liquid film thickness in micro tube slug flow. Int J Heat Fluid Fl 35:842–853

Han Y, Shikazono N (2009b) Measurement of the liquid film thickness in micro square channel. Int J Multiph Flow 30:896–903

Haverkamp V, Ehrfeld W, Gebauer K, Hessel V, Lowe H, Richter T, Wille C (1999) The potential of micromixers for contacting of disperse liquid phases. Fresen J Anal Chem 364:617–624

Hazel AL, Heil M (2002) The steady propagation of a semi infinite bubble into a tube of elliptical or rectangular cross-section. J Fluid Mech 470:91–114

Kreutzer MT, Kapteijn F, Moulijn JA, Heiszwolf JJ (2005a) Multiphase monolith reactors: chemical reaction engineering of segmented flow in microchannels. Chem Eng Sci 60:5895–5916

Kreutzer MT, Kapteijn F, Moulijn JA, Heiszwolf JJ (2005b) Inertial and interfacial effects on pressure drop of Taylor flow in capillaries. AIChE J 51:2428–2440

Lafaurie B, Nardone C, Scardovelli R, Zaleski S, Zanetti G (1994) Modelling merging and fragmentation in multiphase flow with SURFER. J Comput Phys 113:134–147

Leclerc A, Philippe R, Houzelot V, Schweich D, de Bellefon C (2010) Gas–liquid Taylor flow in square microchannels: New inlet geometries and interfacial area tuning. Chem Eng J 165:290–300

Leung SSY, Liu Y, Fletcher DF, Haynes BS (2010) Heat transfer in well-characterised Taylor flow. Chem Eng Sci. doi:10.1016/j.ces.2010.09.014

Liu D, Wang S (2008) Hydrodynamics of Taylor flow in noncircular capillaries. Chem Eng Process 47:2098–2106

Pohorecki R, Kula K (2008) A simple mechanism of bubble and slug formation in Taylor flow in microchannels. Chem Eng Res Des 86:997–1001

Qian D, Lawal A (2006) Numerical study on gas and liquid slugs for Taylor flow in a T-junction microchannel. Chem Eng Sci 61:7609–7625

Renardy Y, Renardy M (2002) PROST: a parabolic reconstruction of surface tension for the volume-of-fluid method. J Comput Phys 183:400–421

Sarrazin F, Bonometti T, Loubière K, Prat L, Gourdon C, Magnaudet J (2006) Experimental and numerical study of droplets hydrodynamics in microchannels. AIChE J 52:4061–4070

Scardovelli R, Zaleski S (1999) Direct numerical simulation of free-surface and interfacial flow. Annu Rev Fluid Mech 31:567–303

Sobieszuk P, Cyganski P, Pohorecki R (2008) Volumetric liquid side mass transfer coefficient in a gas–liquid microreactor. Chem Process Eng 29:651–661

van Steijn V, Kreutzer MT, Kleijn CR (2007) μ-PIV study of the formation of segmented flow in microfluidic T-junction. Chem Eng Sci 62:7505–7514

Taha T, Cui ZF (2006) CFD modelling of slug flow inside square capillaries. Chem Eng Sci 61:665–675

Taylor GI (1961) Deposition of a viscous fluid on the wall of a tube. J Fluid Mech 10:161–165

Triplett KA, Ghiaasiaan SM, Abdel-Khalik SI, Sadowsli DL (1999) Gas–liquid two-phase flow in microchannels. Part i: two-phase flow patterns. Int J Multiph Flow 25:377–394

Völkel N (2009) Design and characterization of gas–liquid microreactors, PhD Thesis, Institut National Polytechnique de Toulouse, France

Waelchli S, von Rohr PR (2006) Two-phase flow characteristics in gas–liquid microreactors. Int J Multiph Flow 32:791–806

Wong H, Radke CJ, Morris S (1995) The motion of long bubbles in polygonal capillaries Part 1:Thin films. J Fluid Mech 292:71–94

Yue J, Chen G, Yuan Q, Luo L, Gonthier Y (2007) Hydrodynamics and mass transfer characteristics in gas–liquid flow through a rectangular microchannel. Chem Eng Sci 62:2096–2108

Yue J, Luo L, Gonthier Y, Chen G, Yuan Q (2008) An experimental investigation of gas–liquid two-phase flow in single microchannel contactors. Chem Eng Sci 63:4189–4202

Yun J, Lei Q, Zhang S, Shen S, Yao K (2010) Slug flow characteristics of gas-miscible liquids in a rectangular microchannel with cross and T-shaped junctions. Chem Eng Sci 65:5256–5263